Universidad Carlos III de Madrid
e-Archivo

Institutional Repository

This document is published in:

*Journal of Alloys and Compounds* (2013). 580, 584-591.
DOI: http://dx.doi.org/10.1016/j.jallcom.2013.07.125

© 2013 Elsevier B.V.

# Structural, morphological and luminescence properties of nanocrystalline up-converting $Y_{1.89}Yb_{0.1}Er_{0.01}O_3$ phosphor particles synthesized through aerosol route

V. Lojpur [a], L. Mancic [a], M.E. Rabanal [b], M.D. Dramicanin [c], Z. Tan [d], T. Hashishin [d], S. Ohara [d], O. Milosevic [a,*]

[a] Institute of Technical Sciences of the Serbian Academy of Sciences and Arts, K. Mihailova 35/IV, 11000 Belgrade, Serbia
[b] University Carlos III of Madrid, Avd. Universidad 30, 28911 Leganes, Madrid, Spain
[c] Vinca Institute of Nuclear Science, University of Belgrade, P.O. Box 522, Belgrade, Serbia
[d] JWRI, Osaka University, 11-1 Mihogaoka, Ibaraki, Osaka 567-0047, Japan
* Corresponding author. Tel.: +381 11 2636994; fax: +381 11 2185263. E-mail address: olivera.milosevic@itn.sanu.ac.rs (O. Milosevic).

**Abstract:** Nanocrystalline up-converting $Y_2O_3$:$Yb^{3+}$, E r $^{3+}$ phosphor particles were processed in a dispersed system-aerosol, generated ultrasonically at 1.3 MHz from common nitrate precursor solution having fixed ytter-bium-to-erbium concentration ratio. The appropriate process parameters: residence time 21 s, carrier gas (air) flow rate 1.6 $dm^3$/min, synthesis temperature 900 °C, led to the formation of un-agglomerated spherical nanostructured secondary particles, having mean particle size of approx 450 nm, composed of primary nanoscaled (20 nm) subunits. In order to reach targeting phase crystallinity, the as-prepared particles were additionally annealed at 1100 °C in air for 12, 24 and 48 h, respectively. Particle structure, morphology and purity were analyzed by X-ray powder diffraction (XRPD), scanning electron microscopy (FESEM/SEM), analytical and high resolution transmission electron microscopy (TEM/HRTEM) in combi-nation with energy dispersive X-ray analysis and Fourier Transform Infrared Spectroscopy (FTIR). All samples crystallized in a cubic bixbyte-structure, space group *Ia*-3. The crystallite size changed with annealing time from 30 nm in as-prepared sample to 135 nm in sample annealed for 48 h, respectively. Emission spectra were assigned to the following trivalent erbium f–f electronic transitions: $^2H_{9/2} \rightarrow {}^4I_{15/2}$ (blue: 407–420 nm), ($^2H_{11/2}$, $^4S_{3/2}$) $\rightarrow {}^4I_{15/2}$ (green: 510–590 nm), and $^4F_{9/2} \rightarrow {}^4I_{15/2}$ (red: 640–720 nm). The significant improvement of the emission decay times were observed after thermal treatment and this effect is correlated further with the structural and morphological particles characteristics. For the anneal-ing time of 12 h a quite high emission decay times were achieved (blue: 0.14 ms, green: 0.32 ms and red: 0.39 ms).

**Keywords**: Aerosol processing, Nanoparticles,$Y_2O_3$ , Up-conversion, Decay time

## 1. Introduction

The up-conversion (UC) describes the physical process which takes multiple photons of lower energy and converts them to one photon of higher energy [1]. In recent years, there is a great interest in the investigation of up-conversion luminescence materials due to the wide range of their applications, such as in solid state lasers, screen displays, sensors, optical data storage, fluorescent labels for sensitive detection of bio-molecules and telecommunications [2–6]. The most commonly used activator is trivalent rare earth ion $Er^{3+}$ since it posses the metastable $^4I_{9/2}$ and $^4I_{11/2}$ levels that can be filled using the low-cost high-power diode laser of 980 nm. Since the absorption of $Er^{3+}$ is quite small at this wavelength, $Yb^{3+}$ ion has been used commonly as a sensitizer to enhance the absorption. Similar positions of energy levels between $^4I_{11/2}$ ($Er^{3+}$) and $^2F_{5/2}$ ($Yb^{3+}$) favors transfer of the excitation energy from $Yb^{3+}$ to $Er^{3+}$ ions, leading to the subsequent excitation of erbium higher levels, so emitting light is with higher energy, i.e. in the visible spectra [7,8].

Since it is well known that up-conversion performance of rare earth ions depends on the host matrix, the choice of suitable host material is of great importance. In accordance to the literature, the following oxides have been investigated up to now: $Y_2O_3$, G d $_2O_3$, $Lu_2O_3$, $ZrO_2$ and $TiO_2$ [9–13]. In particular, rare-earth sesquioxides are well recognized because of their excellent chemical stability, good thermal conductivity and high light output. Especially, $Y_2O_3$ has large energy band gap of 5.8 eV which easily accommodates energy levels of rare earth dopants, while its low phonon energy ($\sim$430–550 $cm^{-1}$) minimizes multiphonon nonradiative relaxations, which is very important for achievement of high emission efficiencies after doping [14]. Moreover, $Y_2O_3$ with its high melting point (2450 °C) and good optical properties (refractive index >1.9

and wide transmission region) is a very suitable host candidate for up-conversion and laser applications [8].

Synthesis of the nanocrystalline host matrix additionally intensifies the luminescence response in comparison to the bulk microcrystalline materials. Because of the localized electronic states and relatively weak ion–phonon interactions, the spectroscopic properties of the divalent and trivalent lanthanide ions in nanocrystals do not differ significantly from those in bulk crystals. However, nanoscale size variation may affect the excited state dynamics including radiative and nonradiative decay times, energy transfer, and thermalization phenomena. Therefore, one expects to observe changes in luminescence decay times, energy transfer efficiency, and efficiency of upconversion luminescence [15].

Different methods for the synthesis of up-conversion nanocrystalline materials are reported in the literature such as sol–gel, combustion, hydrothermal method, pulsed laser deposition and homogenous precipitation method [16–20]. Synthesis of up-convertors with the good characteristics requires strict control of the particle size, morphology, crystal structure and uniform distribution of the luminescent center in the host lattice. Getting the ideal spherical particles is crucial for the good packing density and a small scattering of light, and additionally improves the brightness and resolutions of nanomaterials [21]. In comparison with other methods, aerosol processing offers the possibility for obtaining submicronic nanostructured particles with well controlled size and morphology [22]. The factors that affect the formation of a cer-tain particle structure and morphology are physico-chemical properties of the precursor solution and the mechanisms of its decomposition in a dispersed system-aerosol. The latter one comprises several steps like droplets evaporation and drying, solute precipitation and decomposition, associated with the nucleation, growth, collision and/or coalescence of primary nanoparticles into the secondary spherical assemblage; all of them are influenced by the processing parameters (reaction temperature, atmosphere and residence time). Since the reaction is performed in disperse systems, in the droplets of a few microns, the compositional segregation is suppressed and the uniform distribution of dopants is enhanced.

In our previous work, we have successfully obtained red emitting down-conversion $Y_2O_3$, G d $_2O_3$ and $Y_{1-x}Gd_xO_3$:$Eu^{3+}$ ($x$ = 0–1), phosphor particles with desired morphological and good luminescent properties [23–25]. In addition, we have recently processed the temperature sensitive up-conversion $Y_2O_3$ nanocrystalline particles, doped with $Yb^{3+}$ and co-doped with either $Tm^{3+}$ or $Ho^{3+}$ [26]. Here, ytterbium and erbium co-doped $Y_2O_3$ powders with composition $Y_{1.89}Yb_{0.1}Er_{0.01}O_3$, and with advanced morphological and structural characteristics were synthesized for the first time through aerosol route, i.e. spray pyrolysis, from common nitrate solution. The effects of different annealing conditions on particles structural and morphological characteristics are followed in details and are further correlated with the measured optical properties.

## 2. Experimental

$Y_2O_3$:Yb,Er powder was synthesized *via* spray pyrolysis from 0.1 M nitrate precursor solution containing stoichiometric amounts of $Y(NO_3)_3{\cdot}6H_2O$, $Yb(NO_3)_3{\cdot}5H_2O$ and $Er(NO_3)_3{\cdot}5H_2O$ defined by $Y_{1.89}Yb_{0.1}Er_{0.01}O_3$ composition. Atomization of the precursor was done with an ultrasonic atomizer (RBI-France, working frequency of 1.3 MHz). The aerosol was introduced into a high-temperature tubular reactor with the three independently controlled temperature zones by means of air as a carrier gas, 1.6 $dm^3$/min. The synthesis was carried out on 900 °C and the total droplet/particle residence time in the reactor zone was about 21 s. The as-prepared powder was collected at the end of the reactor in electrostatic precipitator and subjected to the additional thermal treating in air at 1100 °C for 12, 24 and 48 h. The synthesis procedure flowchart is given elsewhere [22].

The phase composition of the obtained powder samples were performed by X-ray powder diffraction (XRPD) analysis on X'Pert Philips diffractometer operating with Cu Kα radiation at 40 mA and 40 kV, in the 2$\theta$ range from 10° to 100° with a step scan of 0.02 and counting time of 10 s per each step. Rietveld structural refinement was done in Topas Academic 4.1 [27]. For the determination of microstructural parameters the Fundamental Parameter Approach was used; FWHM based LVol (volume weighted mean column height) calculation to determine the intermediate crystallite size broadening modeled by a Voigt function and FWHM based strain calculation for the strain broadening was used.

The morphological features and chemical purity were investigated by means of both Scanning (Philips SEM XL30/EDS Dx4) and Field Emission Scanning Electron Microscopy, FESEM (HITACHI SU-70) with energy dispersive X-ray Analysis. For that purpose, the powder samples were dispersed on Cu holder and sputtered with Au (depth layer 2 nm). The particle substructure was analyzed on a 200 kV JEOL-JEM-2100F Transmission Electron Microscopy (TEM) coupled with energy dispersive X-ray Analysis and STEM mode and equipped with ES 500 W CCD camera with electromagnetic lens. Primary particles were identified as individual particles having different contrasts and contour features. Gatan Digital Micrograph™ software package was used for interpretation of HRTEM images.

The infrared absorption spectra were recorded in the range of 4000–400 $cm^{-1}$ on Nickolet spectrophotometer (Model 380, Thermo Nickolet Corporation, Madison, USA). Photoluminescence emission spectra and decay time measurements were performed on spectroflurometer system which comprises optical parametric oscillator excitation source (EKSPLA NT 342, emission range 210–2300 nm), Cryostat (Advance Research Systems DE202-AE) equipped with Lakeshore model 331 controller, spectrograph FHR 1000 (Horiba Jobin–Yvon, 300 groove/mm grating) and ICCD detector (Horiba Jobin–Yvon 3771).

## 3. Results and discussion

X-ray diffraction patterns of as-prepared $Y_{1.89}Yb_{0.1}Er_{0.01}O_3$ (asp) and powders annealed at 1100 °C for a different time are presented in Fig. 1a. All samples have a cubic bixbyte crystal structure, space group *Ia-3*. Reflections of thermally treated samples have much narrower peaks, suggesting the increase in the particle crystallinity with annealing time. Detailed microstructural analysis performed through Rietveld refinement (Table 1, Fig. 1b) revealed small changes in the crystal cell parameters due to the $Yb^{3+}$ and $Er^{3+}$

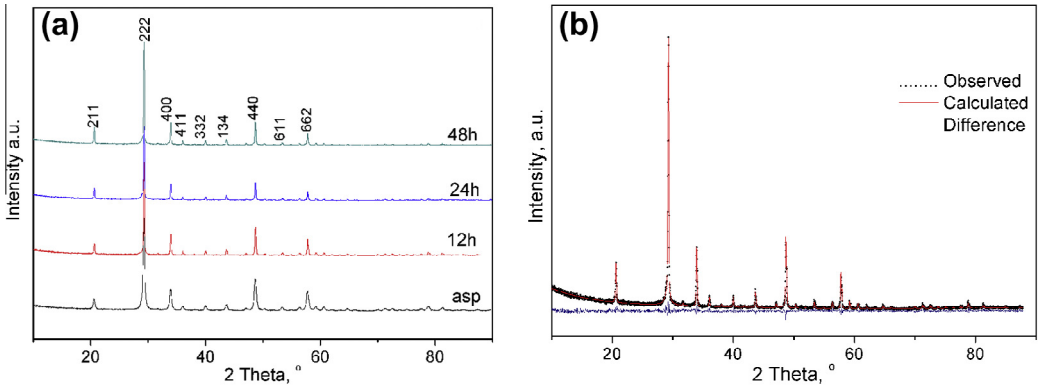


**Fig. 1.** X-ray diffraction patterns of as-prepared $Y_{1.89}Yb_{0.1}Er_{0.01}O_3$ and powders annealed at 1100 °C for 12, 24 and 48 h (a) and Rietveld refinement of sample annealed at 1100 °C for 24 h (b).

**Table 1**
Refined structural parameters of nanocrystalline $Y_{1.89}Yb_{0.1}Er_{0.01}O_3$ powders.

| | Asp | 1100 °C – 12 h | 1100 °C – 24 h | 1100 °C – 48 h |
|---|---|---|---|---|
| Unit cell parameter (Å) | 10.5968 (4) | 10.5983 (3) | 10.5978 (3) | 10.5987 (3) |
| Crystallite size (nm) | 29.7 (7) | 110 (11) | 129 (12) | 135 (17) |
| Microstrain (%) | 0.125 (5) | 0.033 (4) | 0.02 (1) | 0.029 (5) |
| [a]$Y_1$:O bond length (Å) | 2.2100 (71) | 2.193 (11) | 2.167 (14) | 2.189 (13) |
| | 2.2959 (70) | 2.307 (11) | 2.204 (14) | 2.223 (13) |
| | 2.3210 (70) | 2.308 (11) | 2.321 (15) | 2.300 (13) |
| [a]$Y_2$:O bond length (Å) | 2.3009 (72) | 2.323 (11) | 2.421 (15) | 2.397 (13) |
| [a]$Y_1(Y^{3+}, Yb^{3+}, Er^{3+})$ *x* | −0.0314 (1) | −0.0322 (2) | −0.0327 (2) | −0.0326 (2) |
| $O^{2-}$ | | | | |
| *x* | 0.3906 (6) | 0.3915 (9) | 0.3909 (12) | 0.3908 (11) |
| *y* | 0.1520 (7) | 0.1521 (1) | 0.1446 (14) | 0.14482 (12) |
| *z* | 0.3832 (8) | 0.3858 (11) | 0.3957 (15) | 0.39233 (14) |
| $R_{Bragg}$ | 1.408 | 1.959 | 3.181 | 2.661 |
| Goodness of fit | 1.033 | 1.122 | 1.113 | 1.135 |

[a] $Y_1$ corresponds to C2 site; $Y_2$ corresponds to $S_6$ site in cubic crystal unit cell, space group *Ia-3*.

incorporation. As it is well known, the cubic bixbyte-structure of pure $Y_2O_3$ (PDF 89-5591) is characterized with the unit cell parameter of 10.60 Å and coexistence of two nonequivalent crystallographic sites for $Y^{3+}$ ions: non-centrosymmetric $C_2$ at the 24d site and centrosymmetric $S_6$ ($C_{3i}$) at the 8a site [28]. Since both dopants used here have smaller ionic radii in comparison to $Y^{3+}$ ($Y^{3+}$:0.104 Å, $Yb^{3+}$:0.100 Å, $Er^{3+}$:0.103 Å) slight decrease of the lattice parameter is detected in all samples, Table 1. Selective refinement of the $C_2$ and $S_6$ sites occupation with $Y^{3+}$ implies that substitution of $Y^{3+}$ with $Yb^{3+}$ and $Er^{3+}$ ions is more pronounced in the position $C_2$ than in $S_6$ position, i.e. values of 0.9367 for $C_2$ occupation and of 0.9510 for $S_6$ site are obtained (value of 1 corresponds to full site occupation with $Y^{3+}$). In accordance to it, the stoichiometry of as-prepared powder is $Y_{1.8877}Yb_{0.1}Er_{0.01}O_3$ which correlates well with the targeted one ($Y_{1.89}Yb_{0.1}Er_{0.01}O_3$). All powders revealed nanocrystalline particles structure. Average crystallite size of 30 nm is founded in as-prepared sample, while this value increases up to 135 nm in sample annealed for 48 h. Elongation of the heating time also reduces significantly the microstrain in the particles.

Typical morphology of the particles obtained through spray pyrolysis is presented on Fig. 2. Spherical, un-agglomerated particles with the mean particle size of approx 450 nm are visible in the as-prepared powder, Fig. 1a. The influence of prolonged thermal treatment is recognized through the increase of the particle roughness provoked by the crystal growth. As it is shown by XRD analysis the size of the primary crystallites is increased from 30 to 130 nm with heating emphasizing the fact that secondary spherical particles are composed form much smaller nanosized grains. Although the majority of the particles retain their spherical morphology, agglomeration of secondary submicronic particles is also noticeable with annealing time increasing. Consequently, "necks" formation among them due to the sintering process is sporadically found in the sample which is thermally treated for 48 h, Fig. 2d.

FESEM micrographs are presented at Fig. 3 for as-prepared and thermally treated powder samples. The obtained results confirmed SEM observations and the presence of polydispersed spherical particles, sizing below 500 nm. The sponge-like particle morphology is prevailing for the as-prepared powders, as seen at magnification 70,000×. The prolonged heating leads to the better differentiation of primary particles as a result of their thermally induced growth and aggregation. The typical particle morphology after thermal treatment at 1100 °C/24 h is presented at Fig. 3c, showing the blueberry-like structure of secondary particles representing an assembly of nanosized (<50 nm) primary particles. The primary particles are predominantly spherical in shape, colliding to the weak aggregates, as evident from the Fig. 3d.

Based on the elemental analysis (Fig. 4a) it is evident the presence of the following elements: Y (Kα line at 14.9334 and Lα at 1.9226 keV), Er (Lα 6.9488, Mα 1.4057 keV), Yb (Lα 7.4157, Mα 1.5215 keV). The low energy peaks belong to the O (Kα 0.5249) and probably to the C Kα line at 0.277 keV. Cu (Kα 8.040 and Lα 0.930 keV) and Au (Mα 2.12 keV, not signed) peaks belong either

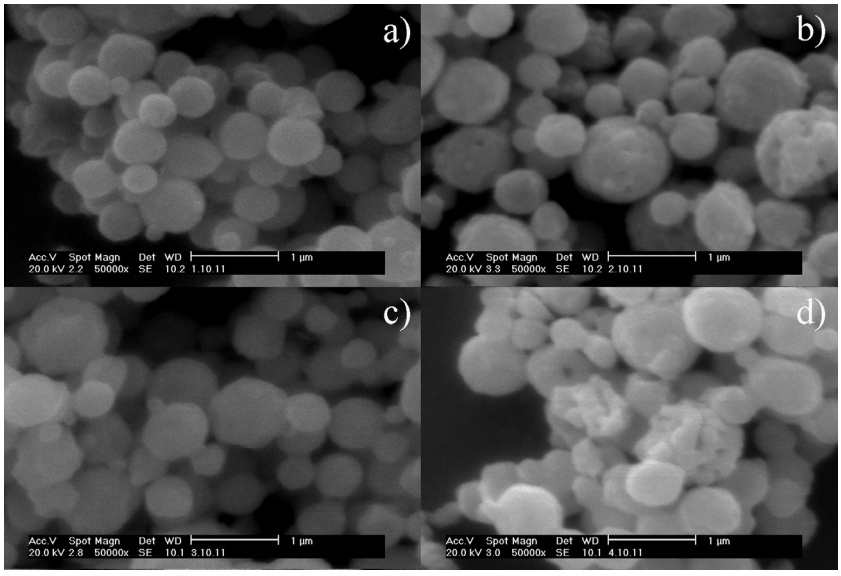


**Fig. 2.** SEM micrographs of as-prepared $Y_{1.89}Yb_{0.1}Er_{0.01}O_3$ (a) and powders annealed at 1100 °C for 12 h (b), 24 h (c) and 48 h (d).

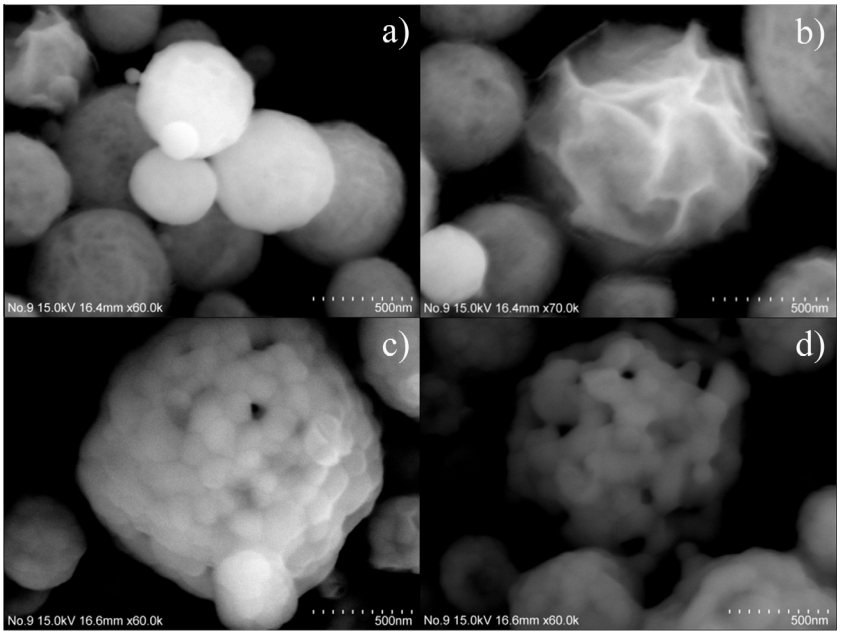


**Fig. 3.** FESEM micrographs of the $Y_{1.89}Yb_{0.1}Er_{0.01}O_3$ powder: as-prepared (a and b) and annealed at 1100 °C/24 h (c and d).

to the holder or to the sputtering layer. The elements distribution is highly homogeneous as followed by the energy dispersive X-ray analysis of the selected rectangular area inside a particle sizing approx. 800 nm (Fig. 4b).

Since the luminescent efficiency of phosphors depends in a great measure of particles purity, Fourier transform infrared emission spectroscopy (FT-IR) is also performed. As shown, FT-IR spectra (Fig. 5) shows sharp peak at 560 $cm^{-1}$ from Y–O bond vibration

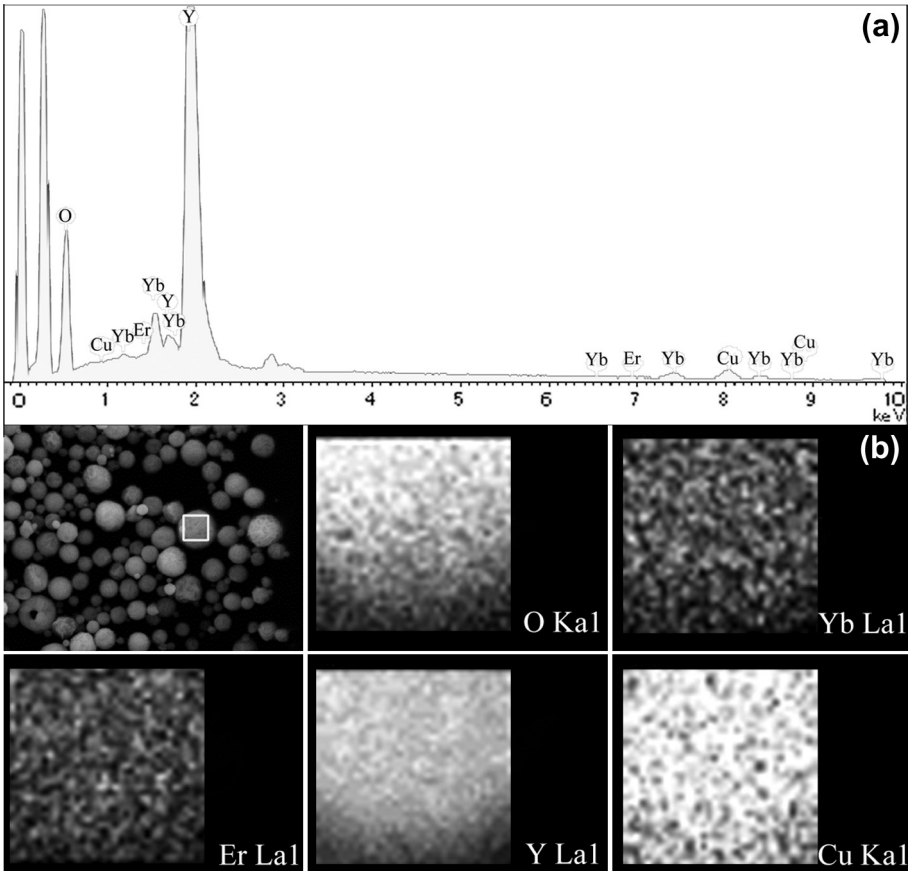


**Fig. 4.** EDAX spectrum (a) and elements distribution inside a particle (b) for the $Y_{1.89}Yb_{0.1}Er_{0.01}O_3$ powder system.

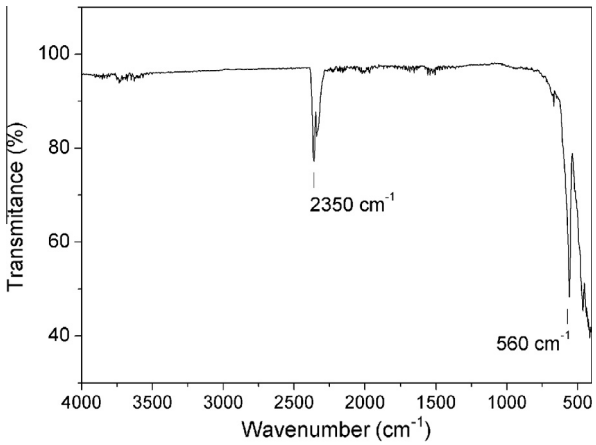


**Fig. 5.** FT-IR spectroscopy of nanocrystalline $Y_{1.89}Yb_{0.1}Er_{0.01}O_3$ powder annealed at 1100 °C for 24 h.

[29] and more important, no presence of residual –OH groups which may quench emission. Peak at 2350 $cm^{-1}$, Fig. 5, is due to physically adsorbed $CO_2$ at the sample surface as a consequence of the measurement environment.

Fig. 6a represents the low magnification bright field TEM image of the approx 600 nm in size secondary particle with the corresponding selected area electron diffraction (SAED) patterns indexed according to the *Ia3* phase (Fig. 6b and c). The crystallized area appears as the dark field. It is evident the particle composite structure and the presence of primary nanoparticles associated with nanoporosity, the former aroused through the collision/coalescence mechanisms during spray pyrolysis [30]. The SAED patterns of the particle inner and at the edge domains imply the particles polycrystalline structure having high defect content. The cubic symmetry, implied by SAED, indicates the interplannar spacings of 0.189 and 0.262 nm corresponding to the 440 and 400 planes, respectively, of a $Y_{1.88}Yb_{0.12}O_3$ compound (JCPDF 87-2368).

Further magnification and contrast analysis of the TEM image in bright field mode of a secondary particle from Fig. 6, reveal small subspheric primary nanoparticles sizing below 20 nm, presented at Fig. 7a. The contrast at the external edge of the secondary parti-cle suggests the presence of approximately 20 nm thick crust at the particle surface. HRTEM analysis (Fig. 7b) shows the presence of well crystallized periodical structures implying the primary particles are with crystalline structure. FFT (Fast Fourier Transform) analysis (Fig. 7c) reveals the interplanar spacings corresponding to the X-ray value for (2 22) and (2 00) planes, respectively, of cu-bic, *Ia-3* phase (file card JCPDF 87-2368, compound type $Y_{1.88}Yb_{0.12}O_3$) as well as to the structure explained by ICSD 84132, the latter used for the XRD structure refinement. This im-plies a very good agreement of the structural data obtained by XRD and TEM analyses. STEM and energy dispersive X-ray analysis

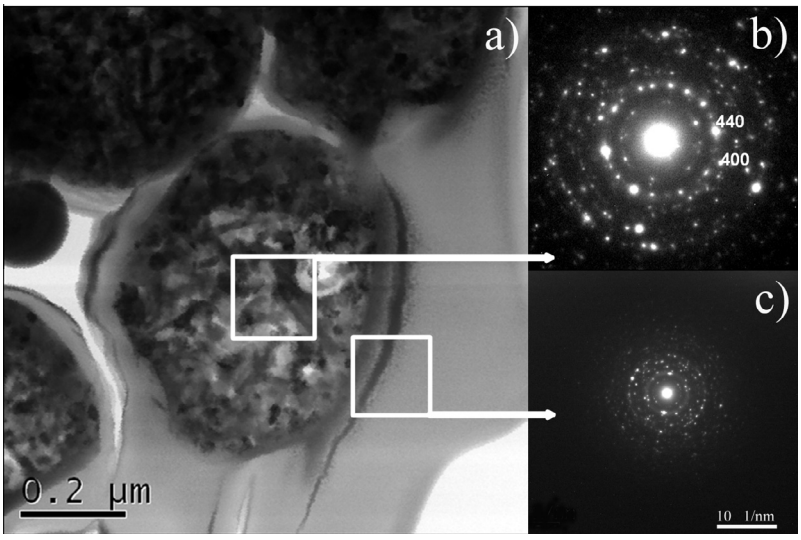


**Fig. 6.** Bright field TEM image of the particle inner structure (a) and the corresponding SAED patterns (b,c).

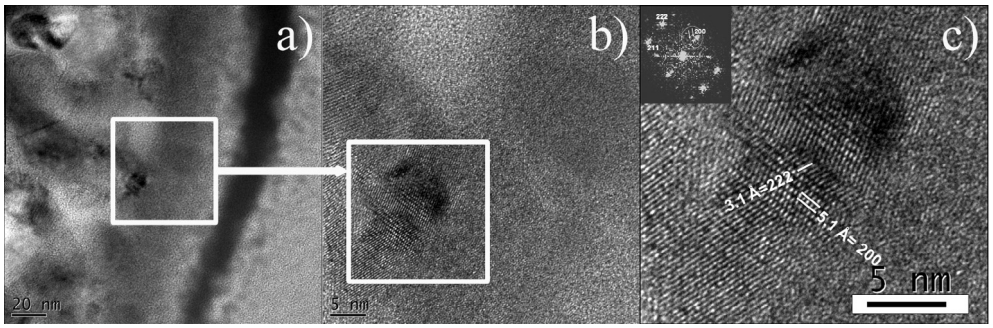


**Fig. 7.** A magnified bright field image from Fig 6 (a) and the corresponding HRTEM lattice image (b) with FFT (c).

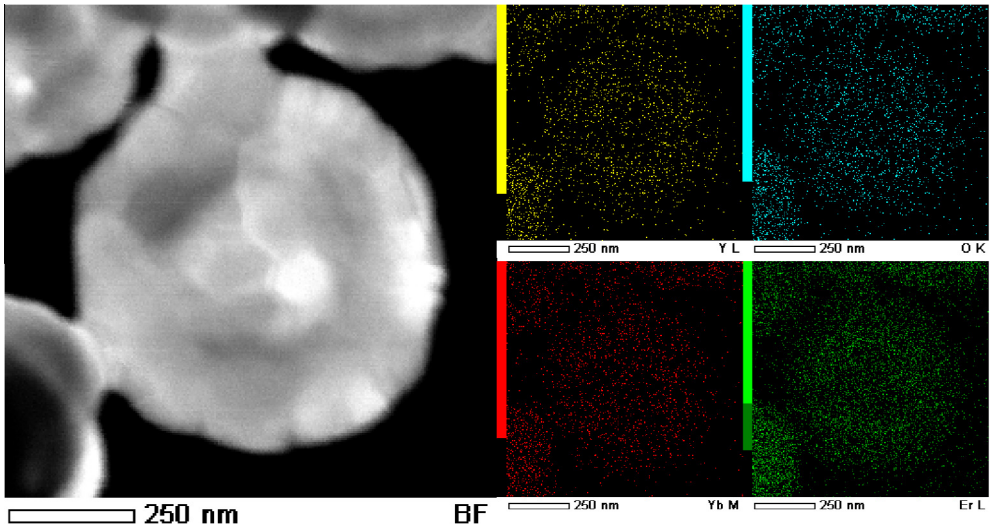


**Fig. 8.** STEM image and EDS mapping of $Y_{1.89}Yb_{0.1}Er_{0.01}O_3$ particles.

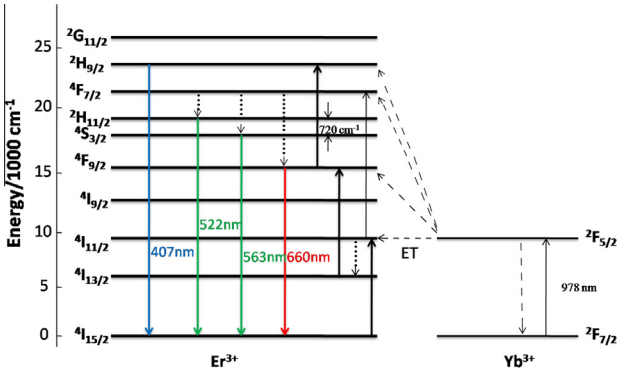


**Fig. 9.** Energy level diagrams of $Yb^{3+}$ and $Er^{3+}$ ions following excitation with 978 nm.

additionally confirmed homogeneous elemental distribution and exclusively presence of yttrium, ytterbium and erbium (Fig. 8)

Up-conversion mechanism in $Yb^{3+}$–$Er^{3+}$ co-doped systems may result from different processes, such as energy transfer up-conversion (ET), excited state absorption (ESA) and addition of photons by energy transfer (APTE) [17]. Schematic diagram of this process is presented in Fig. 9. The energy transfer from excited $Yb^{3+}$ ions promote the state of $Er^{3+}$ from the $^4I_{15/2}$ to the $^4I_{11/2}$ and from $^4I_{11/2}$ to the $^4F_{7/2}$ by excited state absorption. After non-radiative decay to lower energy states ($^2H_{11/2}$, $^4S_{3/2}$ and $^4F_{9/2}$) electrons radiatively de-excite to the ground state giving green and red up-conversion emissions. In the case of blue up-conversion emission, electrons from the $^4I_{11/2}$ level non-radiatively de-excite to $^4I_{13/2}$ and then they are promoted to $^4F_{9/2}$ and $^2H_{9/2}$ by excited state absorption. Blue up-conversion emission is then realized by the radiative de-excitation from $^2H_{9/2}$ level.

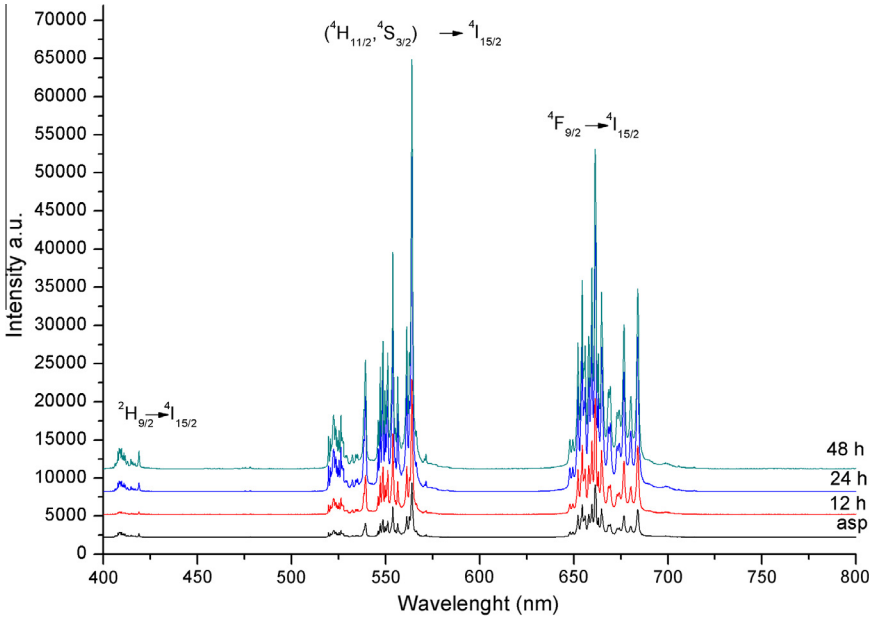


**Fig. 10.** Up-converted spectra of $Er^{3+}$ ions in nanocrystalline $Y_{1.89}Yb_{0.1}Er_{0.01}O_3$ powder excited at 978 nm.

**Table 2**
Decay times of nanocrystalline $Y_{1.89}Yb_{0.1}Er_{0.01}O_3$ powder excited at 978 nm.

| | Decay time (ms) | | |
|---|---|---|---|
| | $^2H_{9/2} \rightarrow {}^4I_{15/2}$ Blue (407 nm) | $^2H_{11/2}$, $^4S_{3/2} \rightarrow {}^4I_{15/2}$ Green (563 nm) | $^4F_{9/2} \rightarrow {}^4I_{15/2}$ Red (660 nm) |
| Asp | 0.06 | 0.27 | 0.23 |
| 12 h | 0.15 | 0.32 | 0.39 |
| 24 h | 0.16 | 0.29 | 0.39 |
| 48 h | 0.15 | 0.29 | 0.35 |

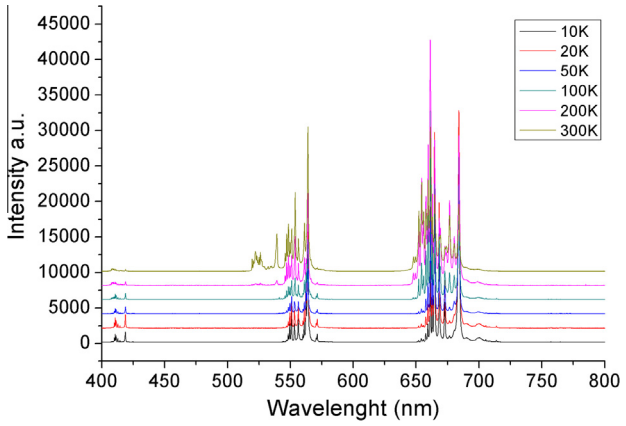


**Fig. 11.** The temperature dependant up-conversion emission of nanocrystalline $Y_{1.89}Yb_{0.1}Er_{0.01}O_3$ powder thermally treated at 1100 °C, 48 h.

The up-conversion luminescence spectra for as prepared and annealed samples of $Y_{1.89}Yb_{0.1}Er_{0.01}O_3$ excited at 978 nm shows blue, green and red luminescence around 407 nm, 563 nm and 660 nm, respectively, Fig. 10. Emission peaks are assigned to the following trivalent erbium f–f electronic transitions: $^2H_{9/2} \rightarrow {}^4I_{15/2}$ (blue: 407–420 nm, three photon process), ($^2H_{11/2}$, $^4S_{3/2}$) $\rightarrow {}^4I_{15/2}$ (green: 510–590 nm, two photon process), and $^4F_{9/2} \rightarrow {}^4I_{15/2}$ (red: 640–720 nm, two photon process) [31]. Since the yttrium oxide structure has two crystallographic six-coordinated sites that could give different Stark splitting of $Er^{3+}$ 4f levels, following transitions are assumed: the $S_6$ lattice with a higher symmetry generates the smallest crystal field so the $Er^{3+}$ ions on this sites experience the smallest Stark splitting (480 $cm^{-1}$) compared to 720 $cm^{-1}$ on the other $Er^{3+}$ ($C_2$) site. For $Er^{3+}$ ions accommodated at $C_2$ site, the f–f transitions are partially allowed by forced electric-dipole transition due to the odd parity terms in the crystal field. On the other hand, for ions situated in the $S_6$ sites of inversion symmetry, only weak magnetic-dipole induced transitions are possible. Therefore, the 4f spectra presented in Fig. 10 exhibit electric dipole transitions from the $Er^{3+}$ ions residing in the $C_2$ sites and magnetic dipole transitions from both sites. The emission bands mostly correspond to $Er^{3+}$ on $C_2$ site whose occupation is more pronounced as it was shown by XRD structural refinement. Increase of the emission intensity with the elongation of heat treatment is observed indicating the improvement of UC efficiency with the rise of the powders crystallinity and the ordering of the crystal lattice. The intensity of the green up-conversion is the most prominent in all samples.

The emission decay times of $Y_{1.89}Yb_{0.1}Er_{0.01}O_3$ powders were measured following excitation at 978 nm, and results are given in Table 2. The lowest value of decay time is detected in as-pre-pared sample because the process parameters (short residence time and high temperature gradient in the reaction zone) favor the formation of defects and retention of microstrains in particles influencing further the luminescent efficiency. With the change of the annealing time, the decay time value of blue emission (407 nm) stay constant, while green (563 nm) and red (660 nm) decay times significantly increase. Red emission decay time prevalence is confirmed in all heat treated samples. The highest value is measured in powder annealed for 12 h. Slight decreases of the decay time with the further prolongation of powders heat treatment is probably related to the observed morphological changes, i.e. agglomeration of particles and appearance of interparticles sintering. The presence of strong green component in spectra indicates very weak ion-pair energy transfer process, implying homogenous distribution of rare-earth ion dopants in the nanocrystalline host matrix [31]. Since it is known that the up-conversion efficiency is mainly influenced by the non-radiative relaxation in material [32], a quite long emission achieved implicates very good up-conversion efficiency of nanocrystalline $Y_{1.89}Yb_{0.1}Er_{0.01}O_3$ powders obtained through spray pyrolysis. The magnitude of up-conversion enhancement achieved in nanocrystalline $Y_{1.89}Yb_{0.1}Er_{0.01}O_3$ powder obtained through spray pyrolysis is about ten times in comparison to the reported values for nanocrystals with the same composition obtained through combustion synthesis ($^4S_{3/2} \rightarrow {}^4I_{15/2}$: 0.011 ms; $^4F_{9/2} \rightarrow {}^4I_{15/2}$: 0.021 ms), and for ~ 30% higher than in bulk ($^4S_{3/2} \rightarrow {}^4I_{15/2}$: 0.25 ms; $^4F_{9/2} \rightarrow {}^4I_{15/2}$: 0.28 ms) [33].

The temperature dependant up-conversion emission of nanocrystalline $Y_{1.89}Yb_{0.1}Er_{0.01}O_3$ powder thermally treated 48 h is presented on Fig. 11, while corresponding decay times are given in the Table 3. The presented results show that synthesized powders exhibit the temperature dependant up-conversion emission. Blue emission has the strongest intensity at 10 K. Up to 200 K the red emission intensities are stronger than green ones while afterwards green emission intensity is the strongest one. The temperature dependence of the $^2H_{11/2} \rightarrow {}^4I_{15/2}$ green emission could be also followed at the temperatures higher than 100 K, when its increasing trend is detected. This feature can be explained by the existence of thermalization process between $^4S_{3/2}$ and $^2H_{11/2}$ levels, separated by an energy gap of about 720 $cm^{-1}$, Fig. 9. When two energy levels

**Table 3**
The temperature dependence of decay times in nanocrystalline $Y_{1.89}Yb_{0.1}Er_{0.01}O_3$ powder thermally treated at 1100 °C, 48 h.

| | Decay time (ms) | | |
|---|---|---|---|
| | $^2H_{9/2} \rightarrow {}^4I_{15/2}$ Blue (407 nm) | $^2H_{11/2}$, $^4S_{3/2} \rightarrow {}^4I_{15/2}$ Green (563 nm) | $^4F_{9/2} \rightarrow {}^4I_{15/2}$ Red (660 nm) |
| 300 K | 0.15 | 0.29 | 0.35 |
| 200 K | 0.15 | 0.29 | 0.34 |
| 100 K | 0.16 | 0.22 | 0.38 |
| 50 K | 0.19 | 0.24 | 0.31 |
| 20 K | 0.15 | 0.30 | 0.27 |
| 10 K | 0.17 | 0.34 | 0.32 |

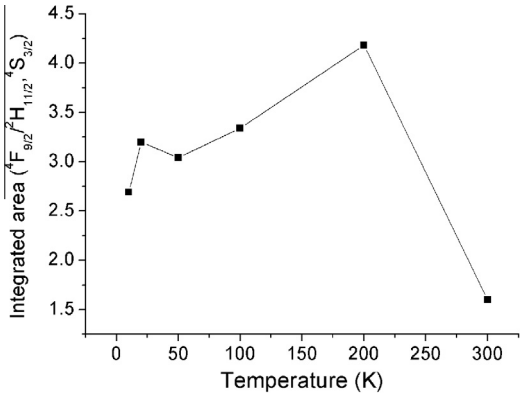


**Fig. 12.** Temperature dependence of the red to green emission integrated area ratio of nanocrystalline $Y_{1.89}Yb_{0.1}Er_{0.01}O_3$ powder thermally treated 48 h.

of the rare earth activator are closely separated by a difference of approximately 1000 $cm^{-1}$, the upper level will not emit the energy at low temperatures due to the high multi-phonon relaxation that quenches it. With the increasing the temperature, the upper level becomes more populated and therefore the emission from this level gradually increases at the expense of the lower level population [34]. In this temperature range the emission bands do not shift in magnitude or direction indicating further that the crystal field splitting occurs on both the $C_2$ and $S_6$ sites.

Calculated values of ratio between integrated areas of red (640–720 nm) and green (510–590 nm) emission (R/G) vs. temperature are presented in Fig. 12. It is clearly evident that at temperatures over 200 K green emission becomes much stronger, but the red emission is still dominant. Observed enhancement of green emission additionally proves that the mechanisms connected with the green up-conversion are temperature dependent.

## 4. Conclusion

It has been demonstrated that ultrasonic aerosol processing may provide spherical, non-agglomerated, approx 450 nm in size $Y_{1.89}Yb_{0.1}Er_{0.01}O_3$ particles with advanced optical properties due to its capability for size and morphology control during synthesis process. This method also suppresses compositional segregation at the droplet level, and therefore more uniform distribution of dopants is achieved. Additional thermal treatment of powders improves further up-conversion efficiency, confirmed by increase of the emission decay times. Observed superior emission decay times are consequence of achieved materials purity and homogeneous doping, and also consequence of modification of a refractive index in effective medium due to the particle nanocrystalline nature.

## Acknowledgements

This research is financially supported through the Project #172035 of the Ministry of Science and Education of the Republic of Serbia. OM especially acknowledge the University Carlos III, Madrid, Spain-Santander Bank Chairs of Excellence program and JSPS 2011/2012 fellowship, Japan.

## References

[1] T. Li, S. Liu, H. Zhang, E. Wang, L. Song, P. Wang, J. Mater. Sci. 46 (2011) 2882–2886.
[2] A.M. Pires, S. Heer, H.U. Güdel, O.A. Serra, J. Fluoresc. 16 (2006) 461–468.
[3] M. Xing, W. Cao, H. Zhong, Y. Zhang, X. Luo, Y. Fu, W. Feng, T. Pang, X. Yang, J. Alloys Comp. 509 (2011) 5725–5730.
[4] Z. Yang, Z. Feng, Z. Jiang, J. Phys. D Appl. Phys. 38 (2005) 1629–1632.
[5] C. Li, B. Dong, C. Ming, M. Lei, Sensors 7 (2007) 2652–2659.
[6] J. Silver, M.I. Martinez-Rubio, T.G. Ireland, G.R. Fern, R. Withnall, J. Phys. Chem. B 105 (2001) 948–953.
[7] H. Guo, N. Dong, M. Yin, W. Zhang, L. Lou, S. Xia, J. Phys. Chem. B 108 (2004) 19205–19209.
[8] A. Martínez, J. Morales, L.A. Díaz-Torres, P. Salas, E. De La Rosa, J. Oliva, H. Desirena, Mater. Sci. Eng. B 174 (2010) 164–168.
[9] A.Og Dikovska, P.A. Atanasov, I.G. Dimitrov, C. Vasilev, T. Kocourek, M. Jelinek, Appl. Surf. Sci. 252 (2006) 4569–4572.
[10] G. Tian, Z. Gu, X. Liu, L. Zhou, W. Yin, L. Yan, S. Jin, W. Ren, G. Xing, S. Li, Y. Zhao, J. Phys. Chem. C 115 (2011) 23790–23796.
[11] O. Meza, L.A. Diaz-Torres, P. Salas, E. De La Rosa, D. Solis, Mater. Sci. Eng. B 174 (2010) 177–181.
[12] B.S. Cao, Y.Y. He, Z.Q. Feng, M. Song, B. Dong, Opt. Commun. 284 (2011) 3311–3314.
[13] J.A. Capobianco, F. Vetrone, J.C. Boyer, A. Speghini, M. Bettinelli, Opt. Mater. 19 (2002) 259–268.
[14] S. Lu, Q. Yang, B. Zhang, H. Zhang, Opt. Mater. 33 (2011) 746–749.
[15] K.A Gschneidner, Handbook on the Physics and Chemistry of Rare Earths 37 Optical spectroscopy, first ed., North-Holland Publ. Co., Amsterdam, 2007.
[16] T.K. Anh, L.Q. Minh, N. Vu, T.T. Huong, N.T. Huong, C. Barthou, W. Strek, J. Lumin. 102–103 (2003) 391–394.
[17] G. De, W. Qin, J. Zhang, J. Zhang, Y. Wang, C. Cao, Y. Cui, J. Lumin. 119–120 (2006) 258–263.
[18] Y.Q. Sheng, J. Liu, L.L. Xu, D. Zhai, Z.G. Zhang, W.W. Cao, Solid State Commun. 150 (2010) 1048–1051.
[19] Y. Li, Y. Zhang, G. Hong, Y. Yu, J. Rare Earths 26 (2008) 450–454.
[20] C. Tan, Y. Liu, Y. Han, W. Li, J. Lumin. 131 (2011) 1198–1202.
[21] H. Guo, Y.M. Qiao, Opt. Mater. 31 (2009) 583–589.
[22] O. Milosevic, L. Mancic, M.E. Rabanal, L.S. Gomez, K. Marinkovic, Kona Powder Part. J. 27 (2009) 84–106.
[23] K. Marinkovic, L. Mancic, L.S. Gomez, M.E. Rabanal, Opt. Mater. 32 (2010) 1606–1611.
[24] O. Milosevic, L. Mancic, M.E. Rabanal, J.M. Torralba, B. Yang, P. Townsend, J. Electrochem. Soc. 152 (2005) G707–G713.
[25] Y. Wang, O. Milosevic, L. Gomez, M.E. Rabanal, J.M. Torralba, B. Yang, P.D. Townsend, J. Phys. Condens. Matter. 18 (2006) 9257–9272.
[26] V. Lojpur, M. Nikolic, L. Mancic, O. Milosevic, M.D. Dramicanin, Ceram. Int. 39 (2013) 1129–1134.
[27] A.A. Coelho, J. Appl. Crystallogr. 36 (2003) 86–95.
[28] J. Silver, M.I. Martinez-Rubio, T.G. Ireland, G.R. Fern, R. Withnall, J. Phys. Chem. B 107 (2003) 1548–1553.
[29] G. Socrates, Infrared and Raman Characteristic Group Frequencies: Tables and charts, third ed., Springer, Berlin, 2004.
[30] M.I. Martín, L.S. Gómez, O. Milosevic, M.E. Rabanal, Ceram. Int. 36 (2010) 767–772.
[31] R.S. Meltzer, S.P. Feofilov, B. Tissue, H.B. Yuan, Phys. Rev. B: Condens. Matter. 60 (1999) R14012–R14015.
[32] X. Luo, W. Cao, Sci. China Ser. B 50 (2007) 505–513.
[33] F. Vetrone, J.-C. Boyer, J.A. Capobianco, A. Speghini, M. Bettinelli, J. App. Phys. 96 (2004) 661–667.
[34] J. Silver, M.I. Martinez-Rubio, T.G. Ireland, R. Withnall, J. Phys. Chem. B 105 (2001) 7200–7204.